EFFECT OF FLAME POWER ON COMBUSTION STABILITY AND EMISSIONS OF A LEAN SWIRLING NH_3/CH_4 FLAME

Phu Nguu Do, Tan Trung Ho*

The University of Danang - University of Technology and Education, Vietnam

*Corresponding author: httrung@ute.udn.vn

(Received: January 20, 2026; Revised: March 19, 2026; Accepted: March 26, 2026)

DOI: 10.31130/ud-jst.2026.24(3).054E

Abstract - This study numerically investigates the combustion behavior and pollutant formation of a lean swirling NH_3/CH_4 flame with a fixed fuel blend of 80% NH_3 and 20% CH_4, under flame powers ranging from 313 to 783 W. Results indicate that increasing flame power elongates the flame and shifts the primary reaction zone downstream, while the peak flame temperature reaches a maximum at 626 W and slightly decreases at higher power. NO_x emissions decrease monotonically with increasing flame power, whereas CO concentrations diminish downstream at higher powers. CO_2 remains concentrated in the high-temperature flame core with minimal sensitivity to flame power. These findings demonstrate that flame power plays a crucial role in regulating flame structure and emissions in swirling NH_3/CH_4 combustion systems.

Key words - NH_3/CH_4 combustion; swirling flame; flame power; non-premixed combustion; emissions

1. Introduction

In the context of the global transition toward carbon neutrality, the development and deployment of carbon-free fuels for industrial combustion systems have become an urgent requirement. Among the potential alternative fuels, ammonia (NH_3) has emerged as a particularly promising candidate due to its carbon-free nature during combustion and its capability to be produced from renewable energy sources [1–4]. Compared to hydrogen (H_2), NH_3 offers distinct advantages in terms of storage and transportation, as it can be liquefied under moderate pressure and can effectively utilize existing industrial infrastructure [5–7]. Nevertheless, the direct utilization of NH_3 as a fuel still faces several challenges, including high ignition energy, low laminar burning velocity, poor flame stability, and high NO_x emissions [8-9]. Consequently, NH_3 is commonly co-fired with more reactive fuels, such as H_2 or CH_4, to enhance combustion characteristics and broaden the stable operating range of ammonia-based flames.

A number of previous studies have investigated the combustion characteristics and emission behaviors of NH_3 and NH_3/CxHy fuel blends in various burner configurations, with particular emphasis on swirl-stabilized combustors. Khateeb et al. [10–11] compared flame stability limits and NO emission trends as a function of global equivalence ratio in premixed swirl burners for NH_3/CH_4 and NH_3/H_2 mixtures, demonstrating that the addition of CH_4 or H_2 is an effective strategy to extend the stable operating window of NH_3 flames. F. H. Vance et al. [12] examined the flashback characteristics of H_2 flames and reported that the flashback limits of premixed H_2/air flames stabilized on slit burners strongly depend on the equivalence ratio and burner geometric parameters, including slit width, slit spacing, and burner plate thickness. Under flashback conditions, the burning velocity is predominantly governed by preferential diffusion effects induced by flame stretch, whereas thermal effects associated with heat transfer between the flame, burned gases, and burner plate play a secondary yet non-negligible role.

Beyond fuel composition, the influence of swirl flow structure on flame stabilization and emission control has also been extensively investigated. Mohd Jaafar et al. [13] demonstrated that the vane angle of the swirl generator significantly affects the size of the central recirculation zone and pressure loss, with a vane angle of 50° providing an optimal balance between flame stability and pressure drop. Soloklou et al. [14] reported that the inlet air diameter ratio and velocity critically govern flame lift-off behavior, flame length, and temperature distribution. An optimal diameter ratio of 0.6 at an air velocity of 0.3 m/s was shown to expand the high-temperature region and improve combustion efficiency.

With respect to fuel–air mixing strategies, Tu et al. [15] conducted a detailed comparison between premixed and non-premixed combustion modes of NH_3/CH_4 mixtures in a swirl-stabilized combustor. Their results indicated that both combustion modes exhibit peak NO emissions at X_{NH3}=40%; however, at the same X_{NH3}, the non-premixed mode consistently produces lower NO emissions. Notably, achieving low NO levels (~300 ppm) requires operation under fuel-rich conditions ($\phi \geq 1.1$) for premixed combustion, whereas near-stoichiometric conditions are sufficient for non-premixed combustion, highlighting its greater operational flexibility.

Overall, previous studies have demonstrated the potential of NH_3 and NH_3/CH_4 blends as viable alternative fuels for industrial combustion systems, while swirl-stabilized combustors have been shown to significantly enhance flame stability and reduce NO_x emissions. However, in most existing works, combustion performance and emission characteristics are strongly coupled with variations in fuel composition, equivalence ratio, and swirl intensity, making it difficult to isolate and independently assess the role of flow dynamics in pollutant formation.

In addition, the study by Yuanping Yang et al. [16] systematically investigated the influence of fuel injection strategies in a tangentially fired swirl combustor using NH_3/CH_4 with O_2/N_2 as the oxidizer. Four configurations were examined: (A) fully premixed, (B) isovelocity non-

premixed, (C) non-isovelocity non-premixed, and (D) centrally injected NH_3 combined with a tangentially swirling CH_4 flame. The results showed that the radial distribution of NO_x is highly sensitive to the fuel injection strategy, with extremely high NO_x concentrations at the combustor center (~3600 ppm at $\phi = 0.5$) for cases A and B. Although case C reduced NO_x emissions, it led to a significant increase in unburned fuel and residual NH_3 emissions. Notably, case D achieved optimal performance, with substantially lower NO_x (~650 ppm) and minimal residual NH_3 (~9 ppm), highlighting the critical role of fuel injection strategy in emission control.

Based on these findings, the present study adopts a non-premixed flame configuration with a dual-row injector consisting of staggered orifices of different diameters (1 mm with 20 holes and 2 mm with 21 holes), replacing the central tubular injection used in case D of [16]. Air is supplied tangentially to generate swirl within the combustor. The fuel composition (NH_3/CH_4 = 80/20 mol%), equivalence ratio (ϕ=0.48), and swirl number are kept constant. Instead of modifying the chemical, the flame power is systematically varied to control the inlet flow momentum and Reynolds number. This approach enables an independent assessment of the influence of flow dynamics, particularly Reynolds-number effects, on flame structure, temperature distribution, and NO_x formation mechanisms in a non-premixed swirl-stabilized combustor.

By decoupling the effects of flow momentum from mixture composition and swirl intensity, this study provides a scientific basis for utilizing operating power as an effective control parameter to reduce NO_x emissions while maintaining stable combustion in ammonia-assisted swirling flames.

Ammonia combustion has emerged as a viable pathway toward carbon-free energy systems. Nevertheless, its practical application, particularly in internal combustion engines, is hindered by its tendency to liquefy under ambient conditions, potentially leading to condensation and fuel line blockage. Such limitations restrict its direct use in conventional engine technologies. As a result, recent research has increasingly focused on ammonia utilization in industrial burners and high-temperature systems, such as furnaces and cement kilns, where fuel handling and phase stability can be more effectively controlled. In this context, the present study advances the current understanding of swirl-stabilized combustors by systematically examining the influence of flow dynamics on emission formation, thereby addressing key practical limitations.

2. Methods

2.1. Combustor geometry and operating conditions

2.1.1. Experimental Setup

The experimental setup comprises two gas cylinders supplying CH_4 and NH_3, an air compressor, a swirl-stabilized combustor, pressure regulators, mass flow controllers, and a camera operating at 60 fps. The CH_4 and NH_3 streams are regulated to a constant pressure of 1 atm and metered individually before being combined through a manifold and injected into the combustor. The air stream is similarly regulated and metered, then distributed into four ducts feeding the swirl vanes to generate a swirling flow for flame stabilization. A camera positioned approximately 20–25 cm from the combustor records the flame for analysis of flame structure and stability under different operating conditions, as shown in Figure 1.

The overall combustor model has a total length of 540 mm and is composed of a plenum section and a combustion chamber. The plenum section accommodates the fuel inlet and the swirl vanes, which are responsible for generating the swirling airflow. The combustion chamber consists of a cylindrical tube with a length of 500 mm and an inner diameter of 55 mm.

Fuel is injected from the bottom of the combustor through a fuel nozzle with an outer diameter of 36 mm, while the combustor body is equipped with four air inlets, each having a diameter of 10 mm, as illustrated in Figure 2.

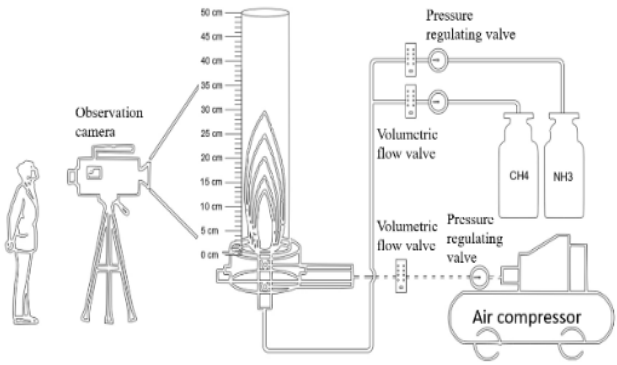

Figure 1. *Layout of the experimental setup*

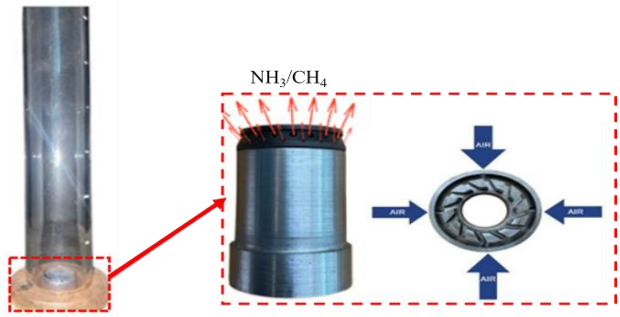

Figure 2. *Experimental model*

The burner design is adapted from a domestic gas stove, featuring 20 large holes and 21 small holes with radii of 2 mm and 1 mm, respectively. In the present configuration, the NH_3/CH_4 fuel mixture is supplied upward through a central nozzle with a diameter of 33 mm, and the combustor body is again provided with four air inlets of 10 mm in diameter.

Air is supplied tangentially through the inlet ducts and guided by the swirl vanes, where it enters the combustion chamber and mixes with the fuel stream. The NH_3/CH_4 fuel mixture is injected upward through the burner holes and subsequently mixes with the swirling air inside the combustion chamber, forming a stabilized swirling flame.

An optimal combination of a relatively large fuel nozzle diameter ratio and a high swirl number has been shown to significantly enhance fuel–air mixing, reduce pressure losses, and improve the overall performance of

combustors. This aspect is particularly critical in gas turbine applications, where swirl-dominated flow plays a decisive role in controlling flame lift-off behavior, combustion intensity, and operational stability. Based on these findings, the present study adopts a combustor configuration characterized by a fuel nozzle diameter ratio of D=0.6 and a swirl vane angle of 60^0 [13–14]. This configuration is regarded as optimal for achieving high flame stability, improved mixing quality, and enhanced combustion performance, as illustrated in Figure 3.

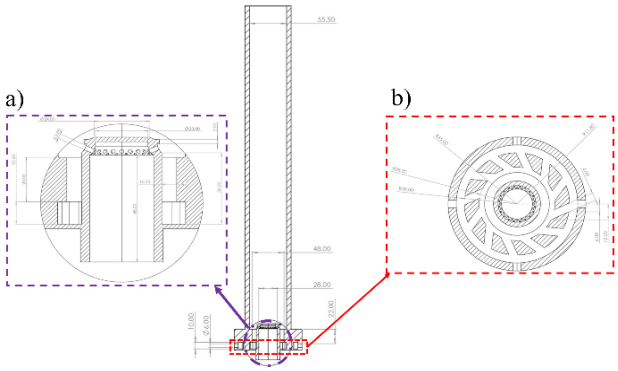

Figure 3. *(a) ratio of fuel diameter to tube diameter; (b) swirl grooves with a 60^0 angle*

Consequently, a non-premixed combustion mode is employed in this study, in which the fuel mixture consists of 80% NH_3 and 20% CH_4 by volume. The fuel–air supply to the combustor is determined and prescribed according to the specified equivalence ratio (ϕ) and flame power, as defined in Eqs. (1) and (4).

The equivalence ratio is determined according to the following expression:

$$\phi = \frac{\left(\frac{A}{F}\right) stoichiometric}{\left(\frac{A}{F}\right) actual} \quad (1)$$

where A and F indicate air and fuel, respectively.

Considering the fuel mixture consisting of 80% NH_3 and 20% CH_4 by mass, the corresponding global combustion reactions of the reactants are expressed as follows:

$$0.8[NH_3+\frac{5}{4\emptyset}(O_2+3.76N_2)]\text{->}NO+\frac{3}{2}H_2O+N_2 \quad (2)$$

$$0.2[CH_4+\frac{2}{\emptyset}(O_2+3.76N_2)]\text{->}CO_2+2H_2O+7.52N_2 \quad (3)$$

$$\text{Flame Power (FE)} = \sum_{k=i}^{n} \dot{m}_i * \text{LHV}_i \text{ (W)} \quad (4)$$

where, m_i denotes the mass flow of the i^{th} fuel component in the mixture, and LHV_i represents its corresponding lower heating value.

Eqs. (2)–(3) are simplified reference reactions introduced exclusively for defining the global equivalence ratio (ϕ), calculating the fuel–air flow rates, and estimating the flame power. These equations are not intended to describe the actual chemical reaction pathways in NH_3/CH_4 combustion, nor do they imply a direct conversion of NH_3 to NO, which in reality occurs through complex intermediate nitrogen chemistry. In the present study, the equivalence ratio ϕ=0.48 is defined as a global equivalence ratio, based on the total fuel and air mass flow rates supplied to the combustor rather than local flame or reaction-zone conditions; the corresponding fuel flow rates are summarized in Table 1.

The study by I.V. Litvinov et al. [17] demonstrates that the swirl number is primarily governed by the geometric characteristics of the swirler. In the present work, a vane-type swirler was designed with an inner diameter of 56 mm, an outer diameter of 78 mm, and a vane angle of 60°. These key geometric parameters, including the swirler dimensions and vane angle, were kept constant across all operating conditions to ensure that the swirl number remained invariant among the investigated cases.

Following the methodology proposed by Ping Wang et al. [18], the Reynolds number (R_e) was evaluated based on the bulk inlet velocity and the characteristic diameter of the inlet duct. In this study, the inlet diameter was fixed at 55.5 mm, while the air flow rate was varied to examine the effect of Reynolds number. This variation resulted in a substantial increase in Reynolds number, whereas the geometric configuration of the swirler and the fuel blending ratio were maintained unchanged.

The lower heating values (LHV) of NH_3 and CH_4 are 18.6 MJ/kg and 50 MJ/kg [19], respectively. All flow rates are reported in units of l/min and were converted to standard conditions, defined as an absolute pressure of 1 atm and a temperature of 20 °C, as summarized in Table 1.

Table 1. *Calculation parameters for the simulation cases*

ϕ	$\dot{m}_{CH4actual}$ (l/min)	$\dot{m}_{NH3actual}$ (l/min)	$\dot{m}_{AIRactual}$ (l/min)	Inlet velocity (m/s)	S_n	R_e	FE (W)
0.48	0.2	0.8	14	0.103	1.5	381	313
	0.4	1.6	28	0.207		762	626
	0.5	2	35	0.259		954	783

As summarized in Table 1, the swirl number (Sn) was maintained constant at 1.5 for all operating conditions. In swirl-stabilized gas turbine combustors, the level of flow turbulence is governed not only by the Reynolds number but also strongly influenced by the swirl intensity. By maintaining a high and invariant swirl number, the present work ensures the persistent presence of swirl-induced turbulence mechanisms, while variations in the Reynolds number primarily reflect changes in operating conditions such as thermal power and inlet flow rate. This approach effectively decouples the influence of swirl intensity from Reynolds number effects, thereby providing clearer insight into the flow dynamics and combustion behavior in swirl-stabilized gas turbine systems.

2.2. Numerical model

Computational Fluid Dynamics (CFD) is based on the numerical solution of the conservation equations of mass, momentum, and energy (Navier–Stokes equations) to simulate fluid flow, heat transfer, and chemical reactions. In this study, CFD is applied to reproduce the swirling flow, fuel–air mixing, and combustion behavior of NH_3/CH_4 mixtures in a swirl-stabilized combustor, allowing detailed analysis of flame characteristics, pollutant formation, and overall combustion performance.

The numerical simulations were performed using ANSYS Fluent under steady-state conditions. The governing equations, including the continuity equation, momentum equations, turbulent kinetic energy equation, energy equation, and radiation equation, were solved using the Reynolds-Averaged Navier–Stokes (RANS) approach in conjunction with the standard k–ε turbulence model. To represent the fast chemical reactions and mass transfer processes in non-premixed combustion, the steady flamelet model based on diffusion flame theory was employed [20, 21]. In the three-dimensional turbulent non-premixed combustion simulations, the governing system consisted of the continuity equation, the RANS equations, the turbulent kinetic energy equations, the energy conservation equation, and the mixture fraction transport equation [22].

The governing equations were discretized using the finite volume method (FVM). A second-order upwind scheme was adopted for the spatial discretization of all transported variables to ensure numerical accuracy. Pressure–velocity coupling was handled using the SIMPLE algorithm, in which the momentum and pressure correction equations were solved in a coupled manner. Convergence was assumed when all normalized residuals dropped below 10^{-6} [23].

The selection of this modeling approach is justified by the simple combustor geometry, the absence of strong curvature effects, and operation under atmospheric pressure conditions (1 atm), in line with previous studies, as illustrated in Figure 4.

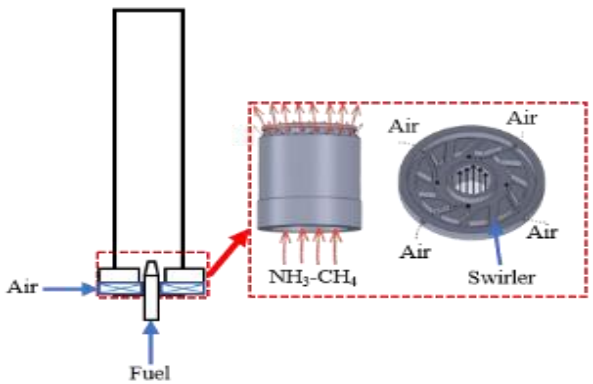

Figure 4. *Numerical model*

Numerous studies have confirmed the applicability of the detailed chemical kinetic mechanism GRI-Mech 3.0 for modeling NO_x formation in ammonia-doped methane combustion under non-premixed conditions. Mino Woo et al. [24] demonstrated that multidimensional CFD simulations based on GRI-Mech 3.0 can reasonably reproduce experimentally observed NO_x emission trends in non-premixed NH_3/CH_4 coflow flames, particularly in cases involving ammonia addition. Similarly, Byung Chul Choi et al. [25] showed that GRI-Mech 3.0 effectively captures fuel-NO formation characteristics and the influence of oxidizer composition in laminar non-premixed ammonia-assisted methane flames.

In addition, comparative studies by Yupeng Zhang et al. [26] reported that, at 0.1 MPa and an ammonia energy fraction of 20%, laminar flame speeds predicted by GRI-Mech 3.0 exhibit trends consistent with experimental data and comparable accuracy to ammonia-specific mechanisms. Furthermore, Xiao Yang et al. [27] found that while different mechanisms predict similar NO trends with increasing ammonia content, GRI-Mech 3.0 tends to predict higher NO levels than experiments, whereas other mechanisms often underpredict NO emissions.

Based on these observations, GRI-Mech 3.0 is adopted in the present study due to its proven capability in capturing NO_x formation trends, its extensive validation in NH_3/CH_4 combustion studies, and its tendency to avoid underestimation of NO emissions [28].

3. Results and discussions

3.1. Mesh generation and independence assessment

3.1.1. Mesh Independence Verification

In this study, 100% CH_4 fuel is employed during the mesh sensitivity analysis to evaluate the influence of mesh resolution on the accuracy of temperature distribution within the combustor and to determine the optimal mesh configuration for the subsequent NH_3/CH_4 combustion simulations.

Figure 5 presents the axial temperature profiles for different mesh configurations, including uniform element sizes of 2 mm, 5 mm, and 10 mm, as well as a hybrid mesh configuration. The results indicate that as the mesh size increases, the predicted combustor temperature also increases. However, within the range of 2 mm to 5 mm, the temperature variation is negligible, demonstrating that the numerical solution has achieved mesh convergence with respect to grid refinement.

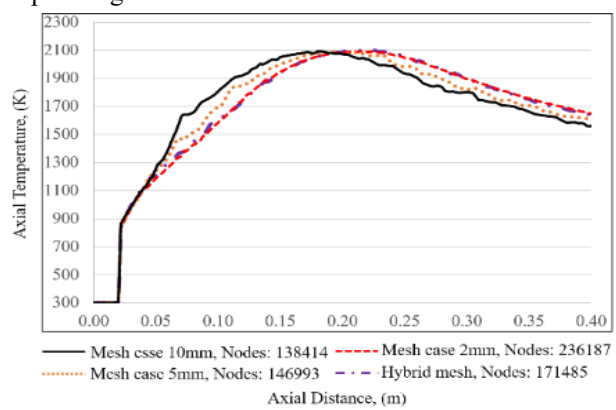

Figure 5. *Evaluation of mesh sensitivity for the swirl-stabilized gas turbine combustor, illustrating center-plane results obtained using multiple mesh densities*

In addition, a hybrid meshing strategy with locally refined cells in the combustion region is evaluated. When the mesh size in the combustion zone is reduced from 10 mm to 5 mm, the resulting temperature profile closely matches that obtained using the 2 mm uniform mesh, highlighting the strong influence of localized mesh refinement on thermal field accuracy.

A comparison of the total node count among different configurations shows that the hybrid mesh contains only about 16% more nodes than the uniform 5 mm mesh, while providing a significantly more stable temperature

distribution that nearly coincides with the 2 mm mesh results. Consequently, the hybrid mesh configuration is selected for all subsequent simulations, consisting of 171485 nodes, and is considered to provide an optimal balance between computational efficiency and numerical accuracy. The customized mesh configuration is illustrated in Figure 6.

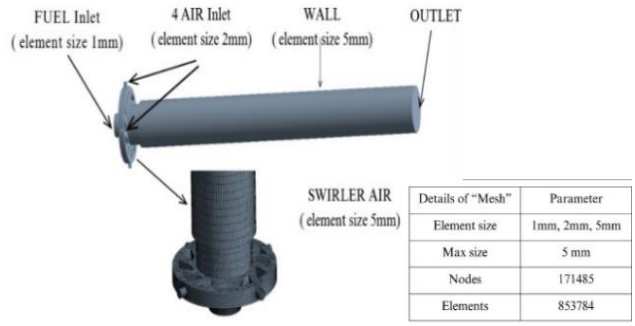

Details of "Mesh"	Parameter
Element size	1mm, 2mm, 5mm
Max size	5 mm
Nodes	171485
Elements	853784

Figure 6. *Mesh parameters of the hybrid mesh*

3.1.2. Validation of Numerical Simulation against Experimental Data

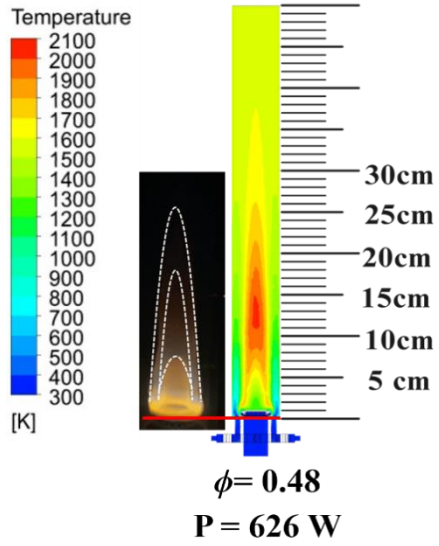

Figure 7. *Comparison between numerical simulation and experiment at a mixing ratio of ϕ=0.48 and P=626 W*

Figure 7 depicts both the numerical and experimental results using an identical vertical scale for the combustion chamber. The numerical predictions reveal a distinct stratification within the flame's temperature field, comprising multiple thermal layers spanning from 300 K to 2100 K. The simulated overall flame height reaches approximately 26 cm, whereas the maximum height of the visible flame sheet observed experimentally is around 24 cm. Based on experimental measurements, the flame core is located at an elevation of approximately 17 cm. This aligns well with the high-temperature zone predicted by the simulation, specifically corresponding to the second orange thermal contour from the top along the temperature probe trajectory. Furthermore, the overall outer envelope of the experimental flame also extends to nearly 24 cm, indicating a substantial similarity in flame morphology and length between the two approaches. Although a minor discrepancy in flame height persists between the numerical and experimental data, this deviation is considered marginal. Consequently, this demonstrates that the developed numerical model is highly capable of capturing the primary characteristics of the flame structure, as well as the governing flow-combustion interactions under the investigated operating conditions.

In the present study, the validation of the numerical model against experimental data is primarily based on a qualitative comparison of flame shape and flame length. Due to experimental limitations associated with measuring the spatial distributions of temperature and species concentrations in non-premixed ammonia-containing flames, a quantitative validation of the local temperature field and NO_x distributions could not be performed. Moreover, numerical modeling inherently involves certain uncertainties, including those related to the selection of chemical kinetic mechanisms and reaction pathways.

Despite these limitations, the modeling framework employed in this study is considered appropriate for the primary objective of the paper, which is to analyze the trends and mechanistic characteristics of NO_x formation in non-premixed NH_3/CH_4 flames. In future work, optimized chemical kinetic mechanisms for ammonia-based fuels will be considered and compared, in combination with more advanced experimental diagnostic techniques, to further improve the quantitative accuracy and overall reliability of the numerical predictions.

3.2. Combustion performance of non-premixed NH_3-CH_4/air flames

3.2.1. Velocity field analysis

Figure 8 presents the velocity contours and streamlines on the central plane of the combustor at different flame power levels, clearly showing the formation of a stable inner recirculation zone (IRZ) induced by strong flow swirling (S_n=1.5>1) in combination with the geometric blockage of the central conical body. The swirl number exceeding unity generates a sufficient radial pressure gradient to cause axial flow reversal, thereby sustaining the IRZ, which is essential for flame stabilization in low-reactivity fuels such as NH_3.

Under a constant equivalence ratio, increasing the flame power raises the Reynolds number from 381 to 954, while the swirl number remains constant. The inlet air velocity correspondingly increases from approximately 2.5 $m \cdot s^{-1}$ to about 5 $m \cdot s^{-1}$ at P=783 W, indicating a substantial enhancement of axial momentum. As the Reynolds number increases, axial inertia progressively dominates over the radial momentum induced by swirl, suppressing the radial expansion of the swirling flow and confining the shear layer toward the flow core. This momentum redistribution leads to a more compact flow structure and a thinner fuel–air mixing layer at higher flame powers. Conversely, at low flame power (P=313 W), the weaker axial momentum allows centrifugal effects associated with S_n >1 to become more influential, promoting radial flow development and resulting in a thicker mixing region located closer to the burner exit.

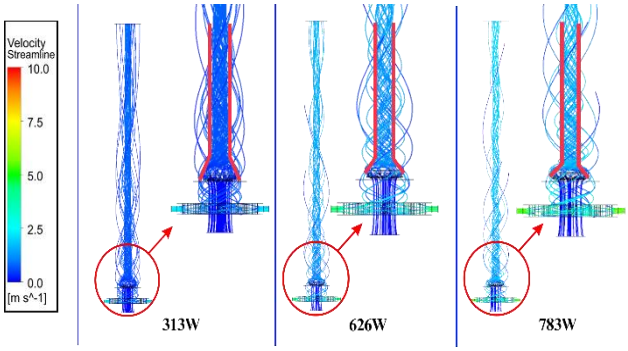

Figure 8. *Axial velocity field distribution along the combustor length at a mixing ratio of ϕ=0.48*

3.2.2. Temperature field analysis

Figure 9 compares the temperature distributions inside the combustor obtained from both numerical simulations and experimental measurements for a fixed equivalence ratio at three different flame power levels. The results indicate that the flame height increases progressively with increasing power, and the location of the thermal core shifts upward and farther away from the burner as the flame power increases.

The region of high temperature also expands with increasing power, forming a broader high-temperature zone. The maximum centerline temperatures are approximately 2014 K at 313 W, 2027 K at 626 W, and 2018 K at 783 W, respectively.

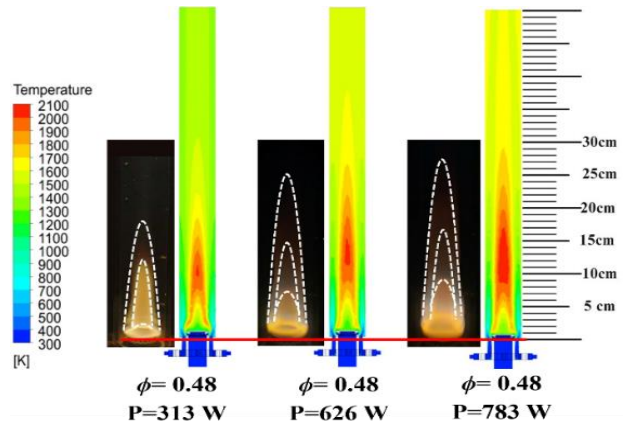

Figure 9. *Axial temperature field distribution along the combustor length at a mixing ratio of ϕ=0.48*

Figure 10 illustrates the axial temperature distributions along the combustor at different flame power levels. The results clearly indicate that both the peak temperature and the extent of the high-temperature region vary significantly with flame power.

At a flame power of P=313 W, the maximum temperature reaches 2014 K at x=10 cm, while the region with temperature ≥1800 K extends only about 7 cm. Under this low Reynolds number condition, the turbulence intensity and momentum diffusion are relatively weak, resulting in a thick fuel–air mixing region concentrated near the burner exit. Consequently, combustion occurs predominantly near the flame root, leading to an early temperature peak but limiting the axial development of the high-temperature zone.

As the flame power increases to P=626 W, the Reynolds number rises substantially, enhancing turbulence intensity and thermal–mass transport. As a result, the reaction zone extends further downstream, with the maximum temperature increasing to 2027 K at x=14 cm, and the temperature ≥1800 K region expanding from 8.5 cm to 22 cm. In addition, the formation of an inner recirculation zone (IRZ), as shown in Figure 8, plays a crucial role in flame stabilization by recirculating hot combustion products toward the flame base.

At the higher flame power of P=783 W, despite the continued increase in Reynolds number, the intensified axial momentum suppresses the radial expansion of the swirling flow, resulting in a thinner mixing layer and a more confined reaction zone. Under this condition, the maximum temperature attains 2018 K at x= 14 cm, which is comparable to the peak-temperature location observed at P=626 W. However, the region characterized by temperatures ≥ 1800 K extends only from 8 cm to 21 cm, corresponding to an axial length of approximately 13 cm, which is slightly shorter than that obtained at P = 626 W. This trend suggests that, at high Reynolds numbers, the dominance of axial momentum constrains radial mixing and limits the spatial development of the reaction zone, thereby inhibiting further axial extension of the high-temperature region despite the increase in flame power.

Overall, the variations in the location and axial extent of the high-temperature region are primarily governed by the influence of the Reynolds number on turbulence intensity, swirl-flow structure, and reaction-zone characteristics. Among the investigated conditions, P=626 W provides the most favorable balance for flame development and stabilization.

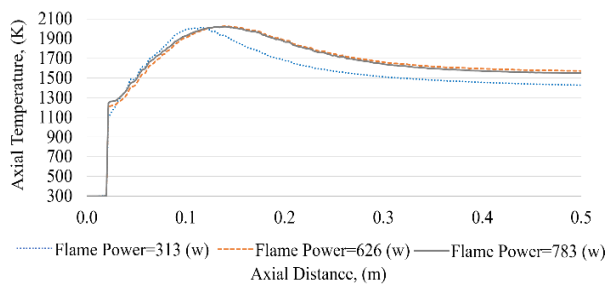

Figure 10. *Axial temperature distribution along the combustor under different flame power conditions*

3.2.3. Emission performance of non-premixed NH_3-CH_4/air flames

a. NO_x Emission performance of non-premixed NH_3-CH_4/air flames

Figures 11 and 12 show the reaction rates of Prompt NO_x and Thermal NO_x at different flame power levels. Prompt NO_x is mainly formed in the early flame region within locally fuel-rich zones, where hydrocarbon radicals react with N_2 to generate intermediate species such as HCN and NH, which are subsequently oxidized to NO. Although Prompt NO_x is generally lower than Thermal NO_x in stationary combustors, its relative contribution becomes more noticeable under moderate-temperature conditions with intense local mixing.

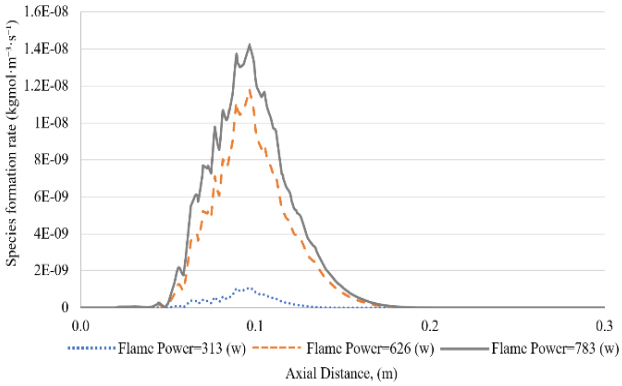

Figure 11. *Axial distribution of prompt NO_x along the combustor*

As illustrated in Figure 11, the Prompt NO_x formation rate peaks at an axial location of approximately 0.1 m, corresponding to the primary reaction zone near the burner exit. At this location, the strong swirling flow (S_n=1.5>1) enhances radial transport and diffusive mixing between CH_4 and air, promoting hydrocarbon radical formation while temperatures remain insufficient for dominant Thermal NO_x pathways. With increasing flame power, the Reynolds number increases and axial momentum becomes more dominant, shifting the main reaction zone downstream and reducing the extent of locally fuel-rich regions. Consequently, Prompt NO_x formation is progressively weakened and becomes more confined at higher flame powers.

As shown in Figure 12, Thermal NO_x is mainly produced through the high-temperature oxidation of atmospheric nitrogen via the extended Zeldovich mechanism, which constitutes the dominant NO_x formation pathway in clean gaseous-fuel combustion. Elevated flame temperatures enhance N_2 dissociation, thereby promoting subsequent reactions with oxygen to form NO_x.

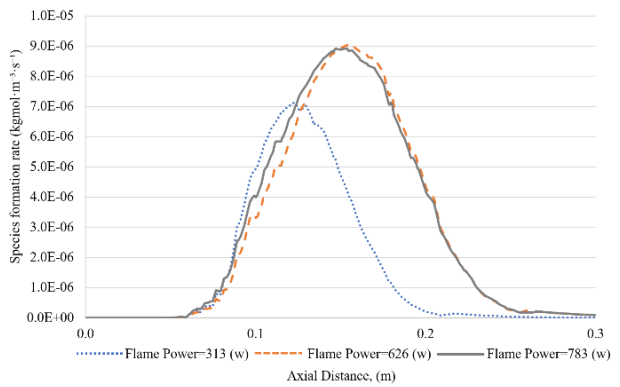

Figure 12. *Axial distribution of thermal NO_x along the combustor*

The results indicate that the onset of Thermal NO_x formation appears earliest at the lowest flame power (P= 313 W), followed by P=783 W and P=626 W. However, the maximum Thermal NO_x reaction rate is observed at P =626 W. This behavior highlights the strong dependence of Thermal NO_x formation on the combined effects of flame temperature and flow characteristics. At higher inlet velocities, the increased Reynolds number intensifies axial momentum and modifies the spatial distribution of high-temperature regions, limiting the extent and continuity of zones favorable for Thermal NO_x reactions despite elevated temperatures. Consequently, an intermediate flame power (P=626 W), where high peak temperatures coincide with a more developed high-temperature region, provides the most favorable conditions for Thermal NO_x formation.

Figure 13 shows that, although the equivalence ratio is maintained constant, NO_x emissions decrease monotonically as the flame power increases from 313 W to 783 W, dropping from 87.1 ppm to 69.0 ppm (approximately 21%), even though the maximum NO_x reaction rate is observed at P=626 W. As summarized in Table 1, higher flame power is accompanied by increased inlet air flow rate and oxygen availability. However, the results in Figures 11–13 indicate that, under non-premixed combustion conditions with nitrogen-containing fuels such as NH_3, the overall NO_x emission trend is governed primarily by the fuel-NO_x formation pathway rather than by local peak reaction intensity.

Increasing flame power leads to a significant rise in inlet velocity and Reynolds number, from R_e=381 to R_e=954, while the swirl number is kept constant (S_n=1.5). The higher Reynolds number strengthens axial momentum and turbulent transport, resulting in a more compact reaction zone and a reduced effective volume of intense fuel–oxidizer interaction in the flame core, where NO_x formation predominantly occurs. From a thermal perspective, the maximum flame temperature reaches its highest value at P=626 W (2027 K), accompanied by the largest axial extent of the high-temperature region (T≥ 1800 K), explaining the locally enhanced thermal NO_x reaction rate under this condition. At the highest flame power (783 W), despite increased oxygen supply and flow momentum, the high-temperature region becomes more spatially confined due to Reynolds-number-dominated flow dynamics, which suppress radial spreading of the swirling flow.

Consequently, although oxidizing conditions become more favorable at higher flame powers, Reynolds-number-controlled flow and mixing effects limit the overall progression of fuel-bound nitrogen oxidation, leading to a monotonic reduction in NO_x emissions with increasing flame power.

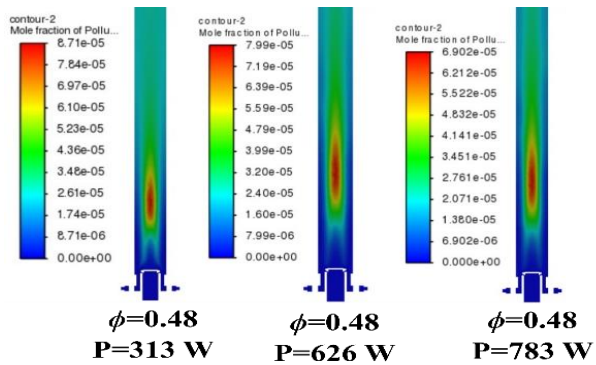

Figure 13. *Axial distribution of NO_x along the combustor in non-premixed NH_3–CH_4/air flames*

b. CO and CO_2 concentrations in non-premixed NH_3–CH_4/air flames

Figure 14 presents the axial distributions of CO concentration in the combustor at different flame powers. Under non-premixed combustion conditions, CO formation and consumption are governed by the balance between partial oxidation of CH_4 and the subsequent oxidation of CO to CO_2. At low flame power (P=313 W), the relatively low inlet velocity and Reynolds number (Re = 381) limit turbulent mixing intensity, leading to locally oxygen-deficient regions near the flame base. As a result, incomplete combustion is promoted, and CO accumulates primarily in the vicinity of the burner exit.

As the flame power increases to 626 W and 783 W, both the inlet velocity and Reynolds number rise significantly (R_e increasing from 762 to 954), accompanied by a corresponding increase in inlet air flow rate and oxygen availability, as summarized in Table 1. Under these conditions, enhanced turbulent mixing improves the interaction between CO and oxidizing radicals, particularly OH, thereby promoting the reaction $CO + OH \rightarrow CO_2 + H$. Consequently, although CO is still generated during the initial oxidation of CH_4, its concentration decreases rapidly along the axial direction after reaching a local maximum near the main reaction zone.

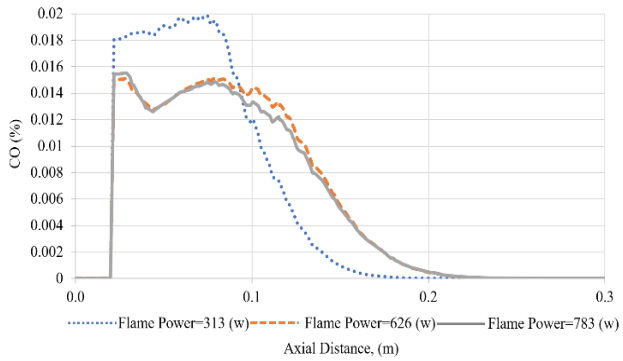

Figure 14. *CO concentration*

Figure 15 illustrates the axial distribution of CO_2 concentration along the combustion chamber. The CO_2 is primarily concentrated within the high-temperature flame core, indicating a high degree of fuel oxidation. At a flame power of 626 W, the maximum CO_2 concentration reaches approximately 0.0248 at an axial position of z=0.17 m. When the flame power is increased to 783 W, a nearly identical peak value (0.0247) is observed at the same axial location. This negligible variation in peak CO_2 concentration suggests that, despite the increases in inlet velocity, Reynolds number, and oxygen supply, the final oxidation of carbon approaches a saturated state under conditions where the equivalence ratio is maintained constant.

When considered together with the CO distributions, the reduction in CO concentration and the invariance of CO_2 levels with increasing flame power can be attributed to enhanced inlet flow velocity, higher Reynolds numbers, and increased oxygen availability. These factors promote more effective turbulent mixing and accelerate the oxidation of CO to CO_2, while simultaneously shortening the region of incomplete combustion in the non-premixed NH_3/CH_4 flame.

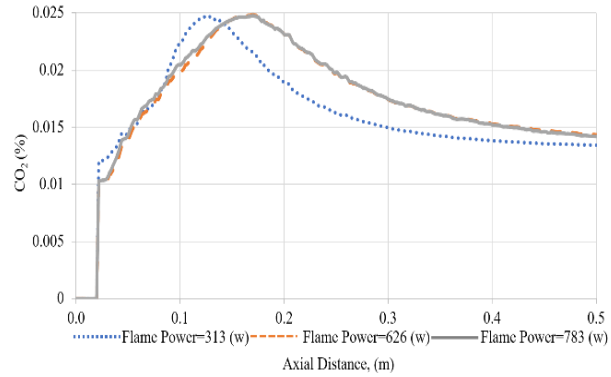

Figure 15. *CO_2 concentration*

4. Conclusion

This study combines experimental measurements and numerical simulations to investigate the effects of flame power on the combustion characteristics and emission behavior of a lean non-premixed swirling NH_3/CH_4 flame (ϕ=0.48; NH_3/CH_4=80/20 mol%). The swirl number was maintained constant at S_n=1.5, while increasing flame power from 313 to 783 W led to a rise in the Reynolds number from 381 to 954.

The results show that increasing flame power elongates the flame and shifts the primary reaction zone downstream as axial momentum becomes increasingly dominant at higher Reynolds numbers. The maximum flame temperature reaches its peak at 626 W and slightly decreases at higher power levels, which is attributed to the modification of local mixing structures caused by enhanced axial inertia under strong swirling conditions. Although higher flame power is associated with increased inlet air velocity and oxygen supply, NO_x emissions decrease from 87.1 ppm to 69.0 ppm. This reduction is primarily linked to changes in the spatial distribution and intensity of high-temperature reaction zones governed by the interplay between Reynolds number and swirl number, which suppresses NO_x formation pathways despite elevated flow rates. The results indicate that fuel-NO_x mechanisms dominate under the present conditions, with flow-induced redistribution of reaction zones exerting a stronger influence than local reaction intensity.

In addition, CO emissions decrease at higher flame power due to enhanced oxidation promoted by increased temperature and mixing intensity, while CO_2 remains mainly concentrated within the high-temperature flame core. Overall, the findings demonstrate that stable combustion with low emissions can be achieved in lean swirling NH_3/CH_4 flames through appropriate control of flame power, providing valuable guidance for the design of low-emission ammonia-fueled combustion systems.

Acknowledgments: This research is funded by Funds for Science and Technology Development of the University of Danang under project number B2023-DN06-05.

REFERENCES

[1] M. A. Nemitallah, M. El-Adawy, G. A. Abdulrahman, S. Mansour, M. A. Habib, and A. Khalifa, "Hydrogen mobility toward affordable and clean energy production in gas turbines: state-Of-the-art and perspectives," *Energy & Fuels*, vol. 39, no. 13, pp. 6045–6077, 2025.

[2] M. El-Adawy, I. B. Dalha, M. A. Ismael, Z. A. Al-Absi, and M. A. Nemitallah, "Review of sustainable hydrogen energy processes: production, storage, transportation, and color-coded classifications," *Energy & Fuels*, vol. 38, no. 23, pp. 22686–22718, 2024.

[3] M. El-Adawy, M. A. Nemitallah, and A. Abdelhafez, "Towards sustainable hydrogen and ammonia internal combustion engines: challenges and opportunities," *Fuel*, vol. 364, Art. no. 131090, 2024.

[4] W. U. Mulk *et al*., "Electrochemical hydrogen production through anion exchange membrane water electrolysis (AEMWE): recent progress and associated challenges in hydrogen production," *International Journal of Hydrogen Energy*, vol. 94, pp. 1174–1211, 2024.

[5] A. Boretti, "Towards hydrogen gas turbine engines aviation: a review of production, infrastructure, storage, aircraft design and combustion technologies," *International Journal of Hydrogen Energy*, vol. 88, pp. 279–288, 2024.

[6] J. H. Kim, J. H. Song, J. W. Ku, Y. H. Kim, and O. C. Kwon, "Combustion characteristics of premixed ammonia-hydrogen/air flames in a swirl model combustor," *International Journal of Hydrogen Energy*, vol. 49, pp. 1075–1086, 2024.

[7] M. El-Adawy *et al*., "Hydrogen-powered aviation: status and perspectives," *Energy & Fuels*, vol. 39, pp. 11469–11503, 2025.

[8] D. K. Madheswaran *et al*., "Ammonia as a hydrogen carrier: a comprehensive analysis of electrolysis efficiency and its potential in sustainable energy systems," *Renewable and Sustainable Energy Reviews*, vol. 221, Art. no. 115915, 2025.

[9] M. Pinzon, R. García-Carpintero, A. R. de la Osa, A. Romero, D. Abad-Correa, and P. Sanchez, "Ammonia as a hydrogen carrier: an energy approach," *Energy Conversion and Management*, vol. 321, Art. no. 118998, 2024.

[10] A. A. Khateeb, T. F. Guiberti, X. Zhu, M. Younes, A. Jamal, and W. L. Roberts, "Stability limits and exhaust NO performances of ammonia-methane-air swirl flames," *Experimental Thermal and Fluid Science*, vol. 114, Art. no. 110058, 2020.

[11] A. A. Khateeb *et al*., "Stability limits and NO emissions of premixed swirl ammonia-air flames enriched with hydrogen or methane at elevated pressures," *International Journal of Hydrogen Energy*, vol. 46, pp. 11969–11981, 2021.

[12] F. H. Vance, L. P. H. de Goey, and J. A. van Oijen, "Development of a flashback correlation for burner-stabilized hydrogen-air premixed flames," *Combustion and Flame*, vol. 243, Art. no. 112045, 2022, doi: 10.1016/j.combustflame.2022.112045.

[13] M. M. Jaafar, K. Jusoff, M. S. Osman, and M. S. A. Ishak, "Combustor aerodynamic using radial swirler," *International Journal of Physical Sciences*, vol. 6, no. 13, pp. 3091–3098, 2011.

[14] M. N. Soloklou and A. A. Golneshan, "Numerical investigation on effects of fuel tube diameter and co-flow velocity in a methane/air non-premixed flame," *Heat and Mass Transfer*, vol. 56, no. 5, pp. 1697–1711, 2020.

[15] Y. Tu, S. Xu, and H. Liu, "Combustion and emission characteristics of NH3/CH4/air in a model swirl combustor: Comparison between premixed and non-premixed modes," *International Journal of Hydrogen Energy*, vol. 48, no. 45, pp. 17311–17323, 2023.

[16] Y. Yang, Q. Huang, J. Sun, P. Ma, and S. Li, "Reducing NO_x Emission of Swirl-Stabilized Ammonia/Methane Tubular Flames through a Fuel-Oxidizer Mixing Strategy," *Energy & Fuels*, vol. 36, pp. 2277–2287, 2022.

[17] I. V. Litvinov, D. A. Suslov, E. U. Gorelikov, and S. I. Shtork, "Swirl number and nozzle confinement effects in a flat-vane axial swirler," *International Journal of Heat and Fluid Flow*, vol. 91, Art. no. 108812, 2021.

[18] P. Wang et al., "Impact of Reynolds number on the flow field structure and NO_x emissions in turbulent NH3-CH4-air flames within a swirl burner," *Applied Thermal Engineering*, Art. no. 127981, 2025.

[19] J. M. Fąfara, "CFD study case of ammonia-hydrogen mixture powered methane gas microturbine combustor in the context of the temperature repartition modifications," *Combustion Engines*, vol. 200, no. 1, pp. 78–86, 2025, doi: 10.19206/CE-197220.

[20] N. Peters, "Laminar diffusion flamelet models in non-premixed turbulent combustion," *Progress in Energy and Combustion Science*, vol. 10, no. 3, pp. 319–339, 1984.

[21] N. Peters, "Laminar flamelet concepts in turbulent combustion," in *Symposium (International) on Combustion*, vol. 21, Elsevier, pp. 1231–1250, 1988.

[22] W. P. Jones and J. H. Whitelaw, "Calculation methods for reacting turbulent flows: a review," *Combustion and Flame*, vol. 48, pp. 1–26, 1982.

[23] Z. Fu, H. Gao, Z. Zeng, J. Liu, and Q. Zhu, "Generation characteristics of thermal NO_x in a double-swirler annular combustor under various inlet conditions," *Energy*, vol. 200, Art. no. 1174, 2020.

[24] M. Woo, B. C. Choi, and A. F. Ghoniem, "Experimental and numerical studies on NO_x emission characteristics in laminar non-premixed jet flames of ammonia-containing methane fuel with oxygen/nitrogen oxidizer," *Energy*, vol. 114, pp. 961–972, 2016.

[25] M. Woo and B. C. Choi, "Numerical study on fuel-NO formation characteristics of ammonia-added methane fuel in laminar non-premixed flames with oxygen/carbon dioxide oxidizer," *Energy*, vol. 226, Art. no. 120365, 2021.

[26] Y. Zhang et al., "Chemical kinetics and numerical simulation of NO emission characteristics in CH4/NH3/air flame," *Reaction Chemistry & Engineering*, vol. 9, no. 6, pp. 1579–1589, 2024.

[27] X. Yang *et al*., "Investigation of NO emission characteristics from co-combustion of methane and ammonia at high-altitude areas," *Journal of Hazardous Materials*, vol. 484, Art. no. 136744, 2025.

[28] M. Frenklach *et al*., "*An optimized detailed chemical reaction mechanism for methane combustion*," Gas Research Institute, Chicago, IL, USA, Tech. Rep. GRI-95/0058, 1995.